JPL Publication D-94645

ECOsystem Spaceborne Thermal Radiometer Experiment on Space Station (ECOSTRESS)

Level-3 Evapotranspiration L3(ET_PT-JPL) Algorithm Theoretical Basis Document

Joshua B. Fisher, ECOSTRESS Science Lead
ECOSTRESS Algorithm Development Team
ECOSTRESS Science Team
Jet Propulsion Laboratory
California Institute of Technology

May 2018
ECOSTRESS Science Document no. D-94645

National Aeronautics and Space Administration

Jet Propulsion Laboratory
California Institute of Technology
Pasadena, California

This research was carried out at the Jet Propulsion Laboratory, California Institute of Technology, under a contract with the National Aeronautics and Space Administration.

Reference herein to any specific commercial product, process, or service by trade name, trademark, manufacturer, or otherwise, does not constitute or imply its endorsement by the United States Government or the Jet Propulsion Laboratory, California Institute of Technology.

© 2018. California Institute of Technology. Government sponsorship acknowledged.

Contacts

Readers seeking additional information about this document may contact the following ECOSTRESS Science Team members:

- Joshua B. Fisher
  MS 233-305C
  Jet Propulsion Laboratory
  4800 Oak Grove Dr.
  Pasadena, CA 91109
  Email: jbfisher@jpl.nasa.gov
  Office: (818) 354-0934

- Simon J. Hook
  MS 183-501
  Jet Propulsion Laboratory
  4800 Oak Grove Dr.
  Pasadena, CA 91109
  Email: simon.j.hook@jpl.nasa.gov
  Office: (818) 354-0974
  Fax: (818) 354-5148

List of Acronyms

ALEXI	Atmosphere–Land Exchange Inverse
ATBD	Algorithm Theoretical Basis Document
Cal/Val	Calibration and Validation
CONUS	Contiguous United States
ECOSTRESS	ECOsystem Spaceborne Thermal Radiometer Experiment on Space Station
ET	Evapotranspiration
EVI-2	Earth Ventures Instruments, Second call
FLiES	Forest Light Environmental Simulator
GEO	Group on Earth Observations
GEWEX	Global Energy and Water Cycle Exchanges Project
GLEAM	Global Land-surface Evaporation: the Amsterdam Methodology
GMAO	Global Modeling and Assimilation Office
HyspIRI	Hyperspectral Infrared Imager
IGBP	International Geosphere-Biosphere Program
iLEAPs	International Land Ecosystem-Atmospheric Processes Study
ISS	International Space Station
L-2	Level 2
L-3	Level 3
LE	Latent heat flux
MERRA	Modern Era Retrospective-Analysis for Research and Applications
METRIC	Mapping EvapoTranspiration at high-Resolution with Internalized Calibration
MODIS	MODerate-resolution Imaging Spectroradiometer
MPI-BGC	Max Planck Institute for Biogeochemistry
NSE	Nash-Sutcliffe Efficiency
PHyTIR	Prototype HyspIRI Thermal Infrared Radiometer
PM-MOD16	Penman-Monteith MOD16
PMBL	Penman-Monteith-Bouchet-Lhomme
PT-JPL	Priestley-Taylor Jet Propulsion Laboratory
RMSD	Root Mean Squared Difference
SDS	Science Data System
SEBS	Surface Energy Balance System
STIC	Surface Temperature Initiated Closure
TIR	Thermal Infrared
VIC	Variable Infilitration Capacity
VIIRS	Visible Infrared Imaging Radiometer Suite
WUE	Water Use Efficiency

Contents

1 Introduction

1.1 Purpose

Evapotranspiration (ET) is one of the primary science output variables by the ECOsystem Spaceborne Thermal Radiometer Experiment on Space Station (ECOSTRESS) mission [*Fisher et al.*, 2014]. ET is a Level-3 (L-3) product constructed from a combination of the ECOSTRESS Level-2 (L-2) Land Surface Temperature (T_s) product [*Hulley* 2015] and Ancillary data products. ET is determined by many environmental and biological controls, including radiative and atmospheric demand, and vegetation physiology, phenology, environmental sensitivity, and productivity [*Fisher et al.*, 2011; *Fisher et al.*, 2017]. ET is sensitive to T_s: plants (and soil) will heat up if they do not have enough water transpiring through their leaf stomata (or soil pores) to cool them down, and vice versa [*Allen et al.*, 2007]. Thus, T_s may be indicative of ET. Nonetheless, while T_s may help determine the change in state of ET, the absolute amount of ET is determined from atmospheric and biological drivers. These drivers are physically described when ET is treated as an energy variable, or the latent heat flux (*LE*), which allows for its calculation based on radiative transfer properties and biological response functions [*Penman*, 1948; *Monteith*, 1965]. Some adaptations to these functions are required when observing the components of the ET calculation from space. In this Algorithm Theoretical Basis Document (ATBD), we describe the approach taken to retrieve ET from space globally, with application to the ECOSTRESS mission.

1.2 Scope and Objectives

In this ATBD, we provide:

1. Description of the ET parameter characteristics and requirements;
2. Justification for the choice of algorithm;
3. Description of the general form of the algorithm;
4. Required algorithm adaptations specific to the ECOSTRESS mission;
5. Required Ancillary data products with potential sources and back-up sources;
6. Plan for the calibration and validation (Cal/Val) of the ET retrieval.

2 Parameter Description and Requirements

Attributes of the ET data required by the ECOSTRESS mission include:

- Spatial resolution of 70 m x 70 m;
- Diurnally varying temporal resolution to match the overpass characteristics of the International Space Station (ISS);
- Latency as required by the ECOSTRESS Science Data System (SDS) processing system;
- Includes all geographic terrestrial regions visible by the ECOSTRESS instrument (i.e., the Prototype HyspIRI Thermal Infrared Radiometer; PHyTIR) from the ISS, with priorities to the ECOSTRESS Science Objective 1 Water Use Efficiency (WUE) target regions ("hotspots"), the ECOSTRESS Science Objective 3 agricultural regions (e.g., the Contiguous United States; CONUS), and the Cal/Val sites.

3 Algorithm Selection

The ET algorithm must satisfy basic criteria to be applicable for the ECOSTRESS mission:

- Physically defensible;
- Globally applicable;
- High accuracy;
- High sensitivity and dependency on remote sensing measurements;
- Relative simplicity necessary for high volume processing;
- Published record of algorithm maturity, stability, and validation.

There are only a few algorithms that satisfy all of these criteria, and they have been the subject of numerous independent rigorous validations and intercomparisons throughout the scientific literature, often under the auspices of the LandFlux Initiative within the Global Energy and Water Cycle Exchanges Project (GEWEX), which is a core component in the World Climate Research Programme (WCRP), and which is linked to the Group on Earth Observations (GEO), the International Land Ecosystem-Atmospheric Processes Study (iLEAPs), and the International Geosphere-Biosphere Program (IGBP). The three primary algorithms under consideration have been: (1) the Priestley-Taylor Jet Propulsion Laboratory (PT-JPL) algorithm [*Fisher et al.*, 2008]; (2) the Penman-Monteith MOD16 (PM-MOD16) algorithm [*Mu et al.*, 2011]; and, (3) the Surface Energy Balance System (SEBS) [*Su*, 2002].

Other approaches, such as Mapping EvapoTranspiration at high-Resolution with Internalized Calibration (METRIC) [*Allen et al.*, 2007] and the Atmosphere–Land Exchange Inverse (ALEXI) [*Anderson et al.*, 2007] have high fidelity, but have typically been more locally (e.g., calibrated to an individual Landsat scene: METRIC) or regionally (e.g., dependent on geostationary observations: ALEXI) focused. ALEXI will be used within ECOSTRESS to address the agricultural-focused Science Objective 3 [*Anderson* 2015]. Other high fidelity global algorithms include the Penman-Monteith-Bouchet-Lhomme (PMBL) approach [*Mallick et al.*, 2013], the Surface Temperature Initiated Closure (STIC) model [*Mallick et al.*, 2014], the Global Land-surface Evaporation: the Amsterdam Methodology (GLEAM) [*Miralles et al.*, 2011], and a global application of ALEXI [*Anderson et al.*, 2013]. These additional global approaches are new and do not satisfy the final criterion required for ECOSTRESS; GLEAM, while having undergone some testing, requires additional measurements of soil moisture and precipitation, thereby unable to satisfy the relative simplicity requirement. Other global approaches include non-physically defensible empirical/statistical upscaling relationships against *in situ* measurements of ET—these include, for example, the Max Planck Institute for Biogeochemistry (MPI-BGC) approach [*Jung et al.*, 2009], artificial neural networks [*Papale and Valentini*, 2003], regression trees [*Zhang et al.*, 2007], support vector models [*Yang et al.*, 2006], and simple regressions [*Wang et al.*, 2007]. Finally, multiple land surface, hydrological, climate, and Earth system models simulate ET globally [e.g., the Variable Infilitration Capacity model (VIC); *Liang et al.*, 1994], but are many degrees removed from the direct remote sensing observations.

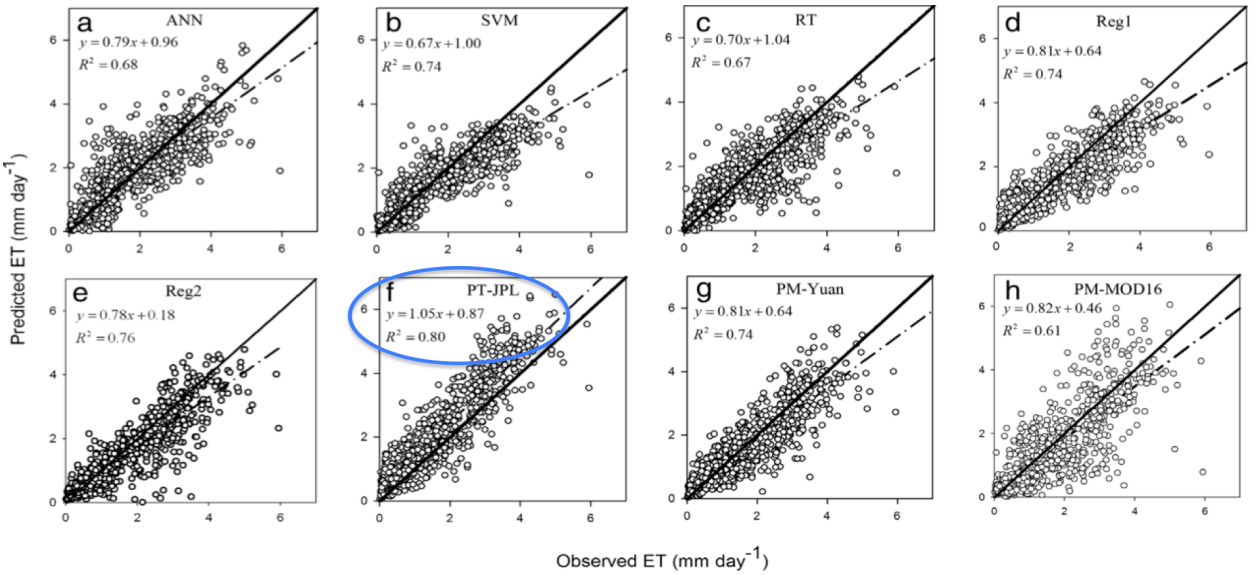

Figure 1. From *Chen et al.* [2014], showing PT-JPL with the highest r^2 and slope closest to 1.0 among multiple ET algorithms across 23 eddy covariance sites.

Three independent evaluations [*Vinukollu et al.*, 2011; *Chen et al.*, 2014; *Ershadi et al.*, 2014] of PT-JPL, PM-MOD16, and SEBS are highlighted here [but, see also, *McCabe et al.*, 2016; *Michel et al.*, 2016; *Miralles et al.*, 2016]. These studies are noteworthy because all algorithms were run with common forcing data, the studies used an extensive set of validation datasets, and they represent independent groups from the US, Australia, and China. The Beijing study used the metrics of correlation coefficient (r^2) and slope of modeled regression against observed ET to determine that PT-JPL exhibited the highest r^2 and slope closest to 1.0 [*Chen et al.*, 2014] (Figure 1). The Princeton study used the metrics of Kendall's τ and Bias to determine that PT-JPL exhibited the highest τ and lowest Bias [*Vinukollu et al.*, 2011] (Figure 2). Finally, the Australia study used the metrics of Nash-Sutcliffe Efficiency (NSE) and Root Mean Squared Difference (RMSD) to determine that PT-JPL exhibited the highest NSE and lowest RMSD [*Ershadi et al.*, 2014]. Given the findings and recommendations of these independent evaluations, in addition to our own expertise in the algorithm development and testing (Figure 3), we selected PT-JPL as the global ET retrieval algorithm for ECOSTRESS.

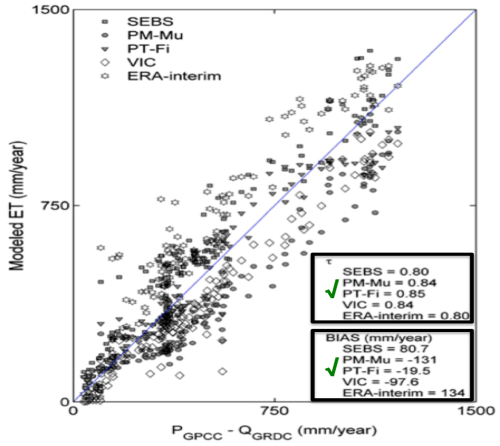

Figure 2. From *Vinukollu et al.* [2011], showing PT-JPL (here, PT-Fi) with the highest τ and lowest bias among multiple ET algorithms.

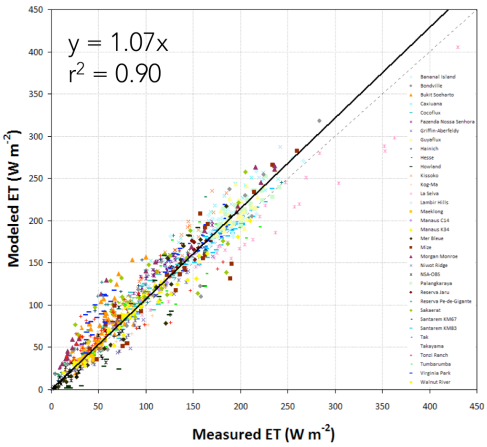

Figure 3. PT-JPL exhibits robust skill from sites across all climates and biome types. [*Fisher et al.*, 2008; *Fisher et al.*, 2009]

4 Evapotranspiration Retrieval: PT-JPL

4.1 PT-JPL: General Form

At the core of the PT-JPL ET algorithm is the potential ET (*PET*) formulation of the Priestley-Taylor [1972] equation, which is a reduced version of the Penman-Monteith [1965] equation, eliminating the need to parameterize stomatal and aerodynamic resistances, leaving only equilibrium evaporation multiplied by a constant (1.26) called the α coefficient:

$$PET = \alpha \frac{\Delta}{\Delta + \gamma} R_n \tag{1}$$

where Δ is the slope of the saturation-to-vapour pressure curve (dependent on near surface air temperature, T_a, and water vapour pressure, e_a), γ is the psychrometric constant, and R_n is net radiation (W m^{-2}). The Priestley-Taylor equation gives the amount of ET that will occur if water is not limiting. *PET* is given in units[1] of R_n, or W m^{-2}, and is therefore considered as an energy variable, i.e., *LE*.

To reduce *PET* to actual ET (*AET*) when water is limiting, *Fisher et al*. [2008] introduced ecophysiological constraint functions (*f*-functions, unitless multipliers, 0-1) based on atmospheric moisture (vapor pressure deficit, *VPD*; and, relative humidity, *RH*) and vegetation indices (normalized difference and soil adjusted vegetation indices, *NDVI* and *SAVI*, respectively). The driving equations in the PT-JPL algorithm are:

$$AET = ET_s + ET_c + ET_i \tag{2}$$

$$ET_c = \left(1 - f_{wet}\right) f_g f_T f_M \alpha \frac{\Delta}{\Delta + \gamma} R_{nc} \tag{3}$$

$$ET_s = \left(f_{\text{wet}} + f_{\text{SM}}(1 - f_{\text{wet}})\right) \alpha \frac{\Delta}{\Delta + \gamma} \left(R_{ns} - G\right) \tag{4}$$

$$ET_i = f_{\text{wet}} \alpha \frac{\Delta}{\Delta + \gamma} R_{nc} \tag{5}$$

where ET_s, ET_c, and ET_i are evaporation from the soil, canopy and intercepted water, respectively, each calculated explicitly and summing to total *AET*. f_{wet} is relative surface wetness (RH[4]) [*Stone et al.*, 1977], f_g is green canopy fraction (f_{APAR}/f_{IPAR}) [*Zhang et al.*, 2005], f_T is a plant temperature constraint (exp(-((T_{max}-T_{opt})/T_{opt})^2)) [*Potter et al.*, 1993; *June et al.*, 2004], f_M is a plant moisture constraint ($f_{APAR}/f_{APARmax}$) [*Potter et al.*, 1993], and f_{SM} is a soil moisture constraint (RH^{VPD}) [*Bouchet*, 1963]. f_{APAR} is absorbed photosynthetically active radiation (PAR), f_{IPAR} is intercepted PAR, T_{max} is maximum air temperature, T_{opt} is T_{max} at max($R_n T_{max} SAVI/VPD$), and G is the soil heat flux. R_{nc}, R_{ns} and G are the net radiation ('*c*' for canopy and '*s*' for soil) and ground heat flux, respectively. No calibration or site-specific parameters are required of this approach.

[1] Water fluxes such as precipitation and *ET* can be given in units of depth per time (i.e., mm·day^{-1}); the units are consistent when they are in volume per area per time (i.e., m^3·ha^{-1}·day^{-1}). 1 m^3 is equal to 1000 litres. Water can also be expressed in units of mass—1 kg of water is equal to 1 mm of water spread over 1 m^2. *ET*, like R_n, can be expressed in units of energy too. Because it requires 2.45 MJ to vaporize 1 kg of water (at 20°C), 1 kg of water is therefore equivalent to 2.45 MJ; 1 mm of water is thus equal to 2.45 MJ·m^{-2}.

Five general data inputs are required to drive the PT-JPL algorithm: 1) R_n; 2) T_a; 3) e_a; 4) surface reflectance in the red (R) band; and, 5) surface reflectance in the near infrared (NIR) band. Midday values averaged over two-week periods (for time steps less than monthly) are used for T_a and e_a to provide stronger coupling between the land and atmosphere. While these data inputs can be obtained from a variety of sources, including satellite observations, *in situ* measurements, and reanalyses, we describe here the approach for obtaining each of these inputs purely from satellite observations, using the MODerate-resolution Imaging Spectroradiometer (MODIS) as the primary source.

The retrieval of R_n involves the integrated retrieval of individual radiation balance components: downwelling shortwave radiation (R_{SD}), upwelling shortwave radiation (R_{SU}), downwelling longwave radiation (R_{LD}), and upwelling longwave radiation (R_{LU}):

$$R_N = (R_{SD} - R_{SU}) + (R_{LD} - R_{LU}) \quad (6)$$

R_{SD} is calculated from an atmospheric radiative transfer model, the Forest Light Environmental Simulator (FLiES) [*Iwabuchi*, 2006; *Kobayashi and Iwabuchi*, 2008; *Ryu et al.*, 2011; *Ryu et al.*, 2012]. FLiES uses: 1) solar zenith angle (5°, 10°, 15°, 20°, 25°, 30°, 35°, 40°, 45°, 50°, 55°, 60°, 65°, 70°, 75°, 80°, 85°); 2) aerosol optical thickness at 550 nm (0.1, 0.3, 0.5, 0.7, 0.9); 3) cloud optical thickness (0.1, 0.5, 1, 5, 10, 20, 40, 60, 80, 110); 4) land surface albedo (0.1, 0.4, 0.7); 5) cloud top height (1000, 3000, 5000, 7000, 9000 m); 6) atmospheric profile type (tropical zone for tropical type, arid and temperate zones for mid-latitude type, snow and ice zones for high-latitude type); 7) aerosol type; and, 8) cloud type. FLiES inputs are provided from MODIS products: MOD04 (aerosol optical thickness, aerosol type), MOD06 (cloud top height, cloud type), MCD43B2 and MCD43B3 (land surface albedo) [*Roesch et al.*, 2004; *Wind et al.*, 2010; *Bi et al.*, 2011; *Chen et al.*, 2011].

R_{SU} is calculated from broadband surface albedo (α), which integrates black and white sky albedo, and R_{SD}:

$$R_{SU} = \alpha R_{SD} \quad (7)$$

R_{LD} is calculated from Stefan-Boltzmann's Law:

$$R_{LD} = \sigma \varepsilon_A T_a^4 \quad (8)$$

where σ is the Stefan-Boltzmann constant (5.67×10^{-8} W m^{-2} K^{-4}), ε_A is the atmospheric emissivity, and T_a is near surface air temperature. ε_A is calculated from total atmospheric precipitable water (ζ) [*Prata*, 1996]:

$$\varepsilon_A = 1 - (1 + \xi) \exp(-(C + D\xi)^{0.5}) \quad (9)$$

where C and D are coefficients with values of 1.2 and 3, respectively. ζ is available from MODIS product MOD05.

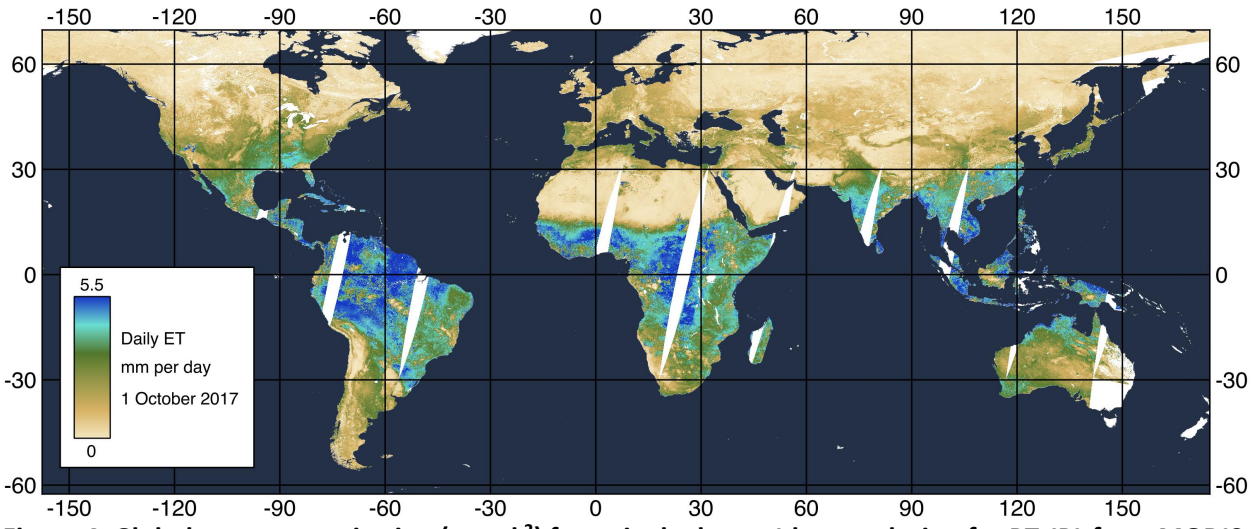

Figure 4. Global evapotranspiration (mm d^{-2}) for a single day at 1 km resolution for PT-JPL from MODIS.

R_{LU} is also calculated from Stefan-Boltzmann's Law:

$$R_{LU} = \sigma \varepsilon_S T_S^4 \tag{10}$$

where ε_S is the surface emissivity and T_S is the radiometric surface temperature in Kelvin. ε_S and T_s are available from MODIS product MOD11L2 [*Coll et al.*, 2009].

Water vapor pressure (e_a) is derived from the dew point temperature (T_D) using the Clausius-Clapeyron relationship between the saturation vapor pressure and temperature:

$$e_a = 6.13753 e^{\left(\frac{17.27 T_D}{T_D + 237.3}\right)} \tag{11}$$

T_D is available from MODIS product MOD07 [*Chen et al.*, 2011].

T_a is retrieved from MOD07 [*Famiglietti et al.*, 2018]. The vertical profiles (Z) are vertically interpolated to surface level using surface pressure (P) and the hypsometric equation with a gas constant of dry air (R) of 287.053 J K^{-1} kg^{-1} and acceleration of gravity (g) of 9.8 m s^{-2}:

$$\mathrm{Z_{lower}} = \frac{R}{g} * (\mathrm{T_{lower}} + 273.16) * log\left(\frac{\mathrm{P_{surface}}}{\mathrm{P_{lower}}}\right) \tag{13}$$

$$\mathrm{Z_{upper}} = \frac{R}{g} * \left(\mathrm{T_{upper}} + 273.16\right) * log\left(\frac{\mathrm{P_{lower}}}{\mathrm{P_{upper}}}\right) \tag{14}$$

such that:

$$T_a = T_{lower} + \left(T_{lower} - \mathrm{T}_{upper}\right) * \frac{Z_{upper}}{Z_{lower}} \tag{15}$$

An example of a single day global retrieval for PT-JPL from MODIS is shown in Figure 4.

4.2 PT-JPL: ECOSTRESS adaptation

Two primary adaptations are applied to PT-JPL to enable its use for the ECOSTRESS mission: (1) adaptation to diurnal cycling; and, (2) spatial resolution improvements.

4.2.1 Diurnal cycling

In the general form of the PT-JPL ET algorithm, this is applied to an instantaneous calculation in time at the time of overpass of the MODIS Terra (or Aqua) instrument, i.e., ~10.30a local time. While the instantaneous retrieval is useful for some applications, more applications require a daily integral or average. What is traditionally done, generally, is to construct a date and latitudinal-varying sinusoidal curve mimicking the sunrise-to-sunset radiation intensity [*Bisht et al.*, 2005]. The relative ratios of the instantaneously observed variables (e.g., the ET-to-R_n ratio, or Evaporative Fraction) are assumed to be held constant throughout that curve/day. Additional refinement may be invoked to include the probabilistic or observed fraction of cloud cover throughout the day and seasonally, land cover or vegetation type-specific parameterizations, and/or dynamically changing relative ratios of the variables of interest.

Because R_n is the dominant driver of ET, and because the other required diurnally-varying PT-JPL drivers also follow closely R_n (i.e., T_a and e_a; fractional vegetation cover and related cover variables are considered diurnally constant), we initialize the diurnal cycle calculation with R_n. *Lagouarde and Brunet* [1993] first developed the framework to obtain the diurnal cycle of T_s from a sinusoidal function with the day length and amplitude equal to the difference between maximum T_s and minimum T_a. *Bisht et al.* [2005] later adapted that to clear sky R_n diurnal cycling:

$$R_n(t) = R_{n,max} sin\left(\pi\left(\frac{t - t_{rise}}{t_{set} - t_{rise}}\right)\right) \tag{16}$$

where $R_{n,max}$ is the maximum value of R_n observed during the given day, and t_{rise} and t_{set} are the local times at which R_n becomes positive and negative, respectively.

The corresponding $R_{n,max}$ for the time of overpass ($t_{overpass}$) is given as:

$$R_{n,max} = \frac{R_{n,overpass}}{sin\left(\pi\left(\frac{t_{overpass} - t_{rise}}{t_{set} - t_{rise}}\right)\right)} \tag{17}$$

The daily average R_n is given as:

$$R_{n,daily} = \frac{\int_{t_{rise}}^{t_{set}} R_n(t)dt}{\int_{t_{rise}}^{t_{set}} dt} = \frac{2R_{n,max}}{\pi} = \frac{2R_{n,overpass}}{\pi sin\left(\pi\left(\frac{t_{overpass} - t_{rise}}{t_{set} - t_{rise}}\right)\right)} \tag{18}$$

The daily-to-instantaneous R_n ratio is therefore:

$$\frac{R_{n,daily}}{R_{n,overpass}} = \frac{1.6}{\pi sin\left(\pi\left(\frac{T-2a}{2T}\right)\right)} \quad (19)$$

where T is day length (i.e., t_{set} minus t_{rise}), and a is the difference in time between when R_n is maximum and when the satellite overpasses. All times use hour of day in local apparent solar time.

For ECOSTRESS, the general form of this equation is applied every day to each of the diurnally-varying R_n drivers (excluding solar zenith angle and T_s and ε_S, the latter two of which are measured at diurnally-varying times of day directly from ECOSTRESS), but the modified instantaneous values are extracted from the equation rather than the daily average.

Similarly, T_a is interpolated diurnally [*Halverson et al.*, 2016]. The wavelength (ω) in radians of the sinusoidal approximation is calculated using the number of daylight hours (DL):

$$\omega = 2\pi\frac{12}{DL} \quad (20)$$

The phase (φ) in radians of the sinusoidal approximation is calculated using the sunrise hour (SH):

$$\varphi = \frac{\pi}{4} - 2\pi\frac{SH}{12} \quad (21)$$

Climatic approximation ($T_{climate}$) of diurnal near-surface air temperature applies these seasonal wavelength and phase values along with known minimum (T_{min}) and maximum (T_{max}) temperatures for a given location on Earth and day of year to calculate air temperature at a target hour in the day (t_{target}):

$$T_{climate} = T_{min} + \frac{T_{max} - T_{min}}{2} * sin\left(\omega * t_{target} + \varphi\right) \quad (22)$$

Calculating the difference between this sinusoidal approximation at the target time of day (t_{target}) and at the time of satellite overpass (t_{obs}) provides an estimation of the increase or decrease in temperature that usually should have occurred over that period of time, which can be added to the remote sensing retrieval (T_{obs}) as a correction to obtain remotely sensed air temperature (T_{target} degrees) at the target time of day:

$$T_{target} = T_{obs} + \frac{T_{max} - T_{min}}{2} * \left(sin\left(\omega * t_{target} + \varphi\right) - sin(\omega * t_{obs} + \varphi)\right) \quad (23)$$

4.2.2 Spatial resolution improvements

The general form of PT-JPL with MODIS given above results in a spatial resolution of 1 km. Incorporation of ECOSTRESS measurements of T_s and e_S at 70 m x 70 m resolution, plus the incorporation of Landsat vegetation cover information (R and NIR) at 30 m resolution, bring the ET retrieval real resolution between 30 m and 1 km, depending whether or not T_s and/or vegetation cover are the dominant drivers of ET for a given place and time (the dominant drivers of ET vary in strength of ET variance explanation in both space and time). For consistency and application, we set the ET spatial resolution to 70 m x 70 m, though we advise caution to users interested in highly heterogeneous surface and meteorological conditions at length scales less than 1 km. All ancillary data at resolutions other than 70 m x 70 m are re-sampled through cubic interpolation to match the ECOSTRESS resolution. In the event that MODIS (or Landsat) data are no longer available for ancillary inputs into PT-JPL during the operational period of ECOSTRESS, alternate data sources are available from the Visible Infrared Imaging Radiometer Suite (VIIRS) at 750 m, and/or, as an ultimate back-up, from NASA's Global Modeling and Assimilation Office (GMAO) Modern Era Retrospective-Analysis for Research and Applications (MERRA), currently at 0.5-0.67° resolution (though likely at finer resolution by the planned flight time of ECOSTRESS.

ECOSTRESS T_s and e_S are incorporated into Equation 10. Landsat-based NDVI and SAVI are incorporated into Equations 3, 4, and 5, including the soil vs. canopy R_n partitioning, as well as f_g, f_M, and T_{opt}. An example of this type of spatial down-scaling approach is given in Figure 5.

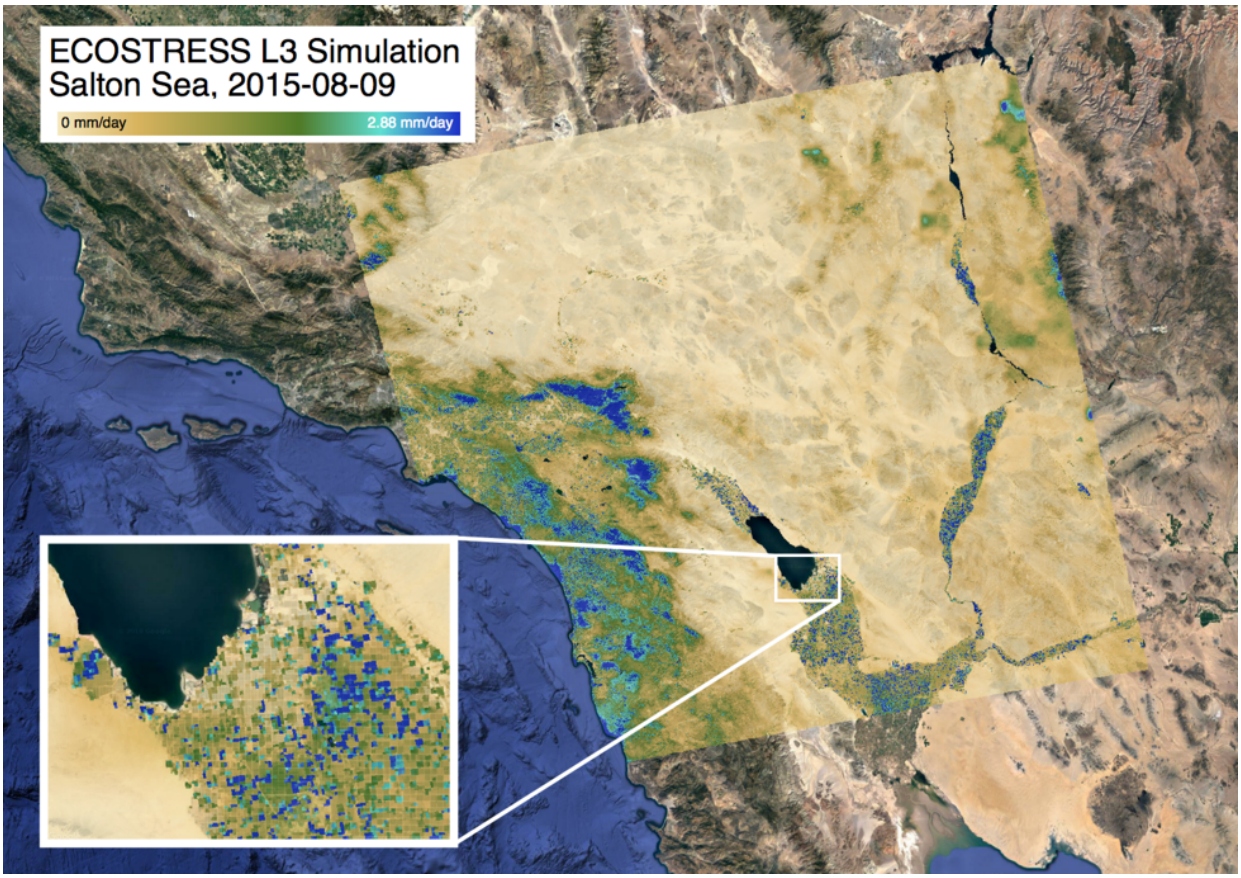

Figure 5. 70 m resolution ET constructed from a blend of 1 km resolution forcing datasets and 70 m resolution datasets shows the ability to detect heterogeneous water uses in a managed landscape.

4.2.3 PT-JPL sensitivity to T_s

The primary sensitivity of PT-JPL to T_s from the ECOSTRESS primary measurement is through R_n, which exerts the dominant control on PT-JPL. We note that there are additional modifications to PT-JPL described throughout the literature that add further sensitivity to T_s through other parts of the algorithm. These developments are still in research-mode, and are not considered in the primary PT-JPL implementation within ECOSTRESS, but described below for reference. This form of PT-JPL was described in *García et al.* [2013], where f_{SM} is replaced by the normalized Apparent Thermal Inertia (*ATI*) index [*Price*, 1977]:

$$ATI = C\frac{1-\alpha}{T_{s,max}-T_{s,min}} \tag{24}$$

$$C = sin\vartheta sin\varphi(1-tan^2\vartheta \cdot tan^2\varphi) + cos\vartheta \cdot cos\varphi \cdot arccos(-tan\vartheta \cdot tan\varphi) \tag{25}$$

where ϑ is latitude, and φ is solar declination [*Iqbal*, 2012].

The modified f_{SM} is thus given as:

$$f_{SM,ATI} = \frac{ATI - ATI_{min}}{ATI_{max} - ATI_{min}} \tag{26}$$

A second modification to PT-JPL's f_M function provides additional sensitivity to T_s following the *ATI*:

$$f_{M,ATI} = (1 - e^{logATI})\frac{f_{APAR}}{f_{APAR,max}} \tag{27}$$

A final modification to PT-JPL's ET_s is through the inclusion of an additional *f*-multiplier, called the soil temperature constraint (f_{ST}):

$$f_{ST} = e^{-\left(\frac{T_s-20}{20}\right)^2} \tag{28}$$

5 Calibration/Validation

ET is measured *in situ* using the eddy covariance technique at hundreds of sites around the world (FLUXNET) [*Baldocchi et al.*, 2001; *Baldocchi*, 2008]. Instruments attached to towers extending above the canopies measure ET over ~1 km integrated footprints (Figure 6), 10 times per second (averaged to 30 minute intervals) year round, thereby enabling direct comparisons to remote sensing observations at similar or finer spatial resolutions [*Jung et al.*, 2009]. After making the necessary *in situ* corrections to anomalous measurements, and ensuring energy balance closure [*Goulden et al.*, 1996; *Fisher et al.*, 2007], the eddy flux measurements may be directly comparable. The FLUXNET sites generally cover most climate zones and biome types, though they are distributed more towards those zones and types within developed countries such as the US and in Europe (Figure 7).

Figure 6. Evapotranspiration is measured directly via the eddy covariance technique from instruments attached to towers extending above canopies, which allows for relatively large-scale integrated measurements over ~1 km footprints.

We selected a subset of FLUXNET sites representing a relatively even distribution across the broad IGBP biome classification types (Table 1). ET measurements will be retrieved from these sites through the central FLUXNET repository—fluxdata.org—or directly from the site PIs. The ECOSTRESS instantaneous ET retrieval will be compared directly to the 30 min instantaneous FLUXNET ET measurement. Bias and root mean squared error (RMSE) statistics will be calculated, and the entire ECOSTRESS ET data product will be bias-adjusted with potentially additional adjustments to further reduce RMSE. These adjustments may be applied universally, or specific to climate zones and biome types, depending on whether or not there are significant bias and RMSE differences between climate zones and biome types.

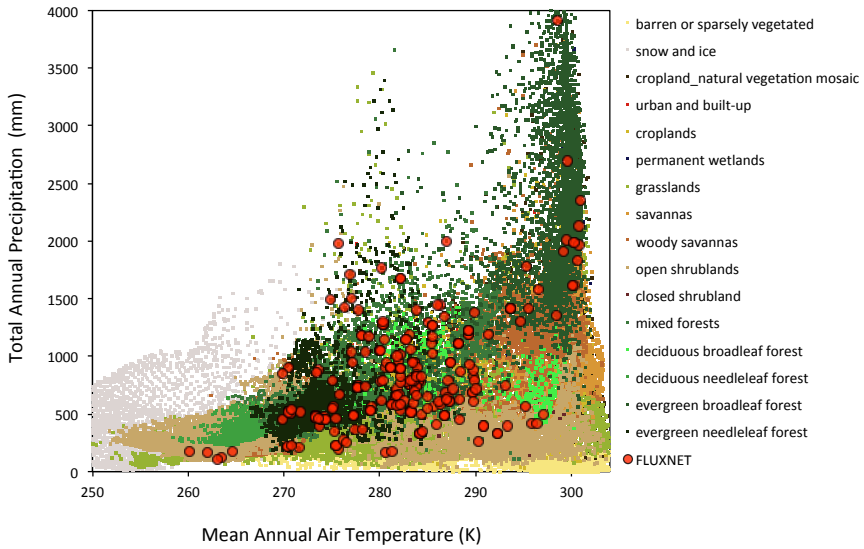

Figure 7. The FLUXNET network of eddy covariance towers span most biome types and climate zones, thereby enabling adequate global sampling of evapotranspiration.

Table 1. ECOSTRESS L3 ET FLUXNET validation sites. ENF: evergreen needleleaf forest; EBF: evergreen broadleaf forest; WSA: woody savanna; SAV: Savanna; CRO: cropland; DBF: Deciduous Broadleaf Forest; Cal/Val: LST Calibration/Validation.

Site	Biome Type	Latitude	Longitude
Campbell River, Canada	ENF	49.9	-125.3
Hartheim, Germany	ENF	47.9	7.6
Howland Forest, ME, USA	ENF	45.2	-68.7
Metolius, OR, USA	ENF	44.5	-121.6
Quebec Boreal, Canada	ENF	49.7	-74.3
Tatra, Slovak Republic	ENF	49.1	20.2
Wind River Crane, WA, USA	ENF	45.8	-122.0
Guyaflux, French Guyana	EBF	5.3	-52.9
La Selva, Costa Rica	EBF	10.4	-84.0
Manaus K34, Brazil	EBF	-2.6	-60.2
Santarem KM67, Brazil	EBF	-2.9	-55.0
Santarem KM83, Brazil	EBF	-3.0	-55.0
Chamela, Mexico	DBF	19.5	-105.0
Duke Forest, NC, USA	DBF	36.0	-79.1
Hainich, Germany	DBF	51.1	10.5
Harvard Forest, MA, USA	DBF	42.5	-72.2
Hesse Forest, France	DBF	48.7	7.1
Tonzi Ranch, CA, USA	DBF/WSA	38.4	-121.1
ARM S. Great Plains, OK, USA	CRO	36.6	-97.5
Aurade, France	CRO	43.5	1.1
Bondville, IL, USA	CRO	40.0	-88.3
El Saler-Sueca, Spain	CRO	39.3	-0.3
Mead 1, 2, 3 NE, USA	CRO	41.2	-96.5

6 Mask/Flag Derivation

For T_s and e_s, the ECOSTRESS L2 flags are used to provide quality information for the L3 ET product. Additional quality flags are incorporated from those provided by the ancillary MODIS products (Table 2):

Table 2. ECOSTRESS L3 ET MODIS ancillary data flags and responses to poor quality.

Input product	Quality Flag	Response to poor quality
MODIS Aerosol	Quality assurance	Replace with assumed minimum AOT 0.005
MODIS Albedo	Quality assurance	Gap-fill Landsat with MODIS and with climatic means
MODIS Cloud	Quality assurance	Replace with zero
MODIS Atmospheric Profile	Quality assurance	Air temperature and dew point are 15-day means
MODIS fPAR, LAI	N/A	Replace with zero
MODIS Land Cover	N/A	N/A
MODIS NDVI	N/A	Gap-fill Landsat with MODIS

7 Metadata

- unit of measurement: Watts per square meter (W m^{-2})
- range of measurement: 0 to 3000 W m^{-2}
- projection: ECOSTRESS swath
- spatial resolution: 70 m x 70 m
- temporal resolution: dynamically varying with precessing ISS overpass; instantaneous throughout the day, local time
- spatial extent: all land globally, excluding poleward ±60°
- start date time: near real-time
- end data time: near real-time
- number of bands: not applicable
- data type: float
- min value: 0
- max value: 3000
- no data value: 9999
- bad data values: 9999
- flags: quality level 1-4 (best to worst)

8 Acknowledgements

We thank Gregory Halverson, Laura Jewell, Gregory Moore, Caroline Famiglietti, Munish Sikka, Manish Verma, Kevin Tu, Alexandre Guillaume, Kaniska Mallick, Youngryel Ryu, and Hideki Kobayashi for contributions to the algorithm development described in this ATBD.

9 References

Allen, R. G., M. Tasumi, and R. Trezza (2007), Satellite-based energy balance for mapping evapotranspiration with internalized calibration (METRIC)-model, *J. Irrig. Drain. E.*, *133*, 380-394.

Anderson, M. C., J. M. Norman, J. R. Mecikalski, J. A. Otkin, and W. P. Kustas (2007), A climatological study of evapotranspiration and moisture stress across the continental United States based on thermal remote sensing: 1. Model formulation, *J. Geophys. Res.*, *112*(D10), D10117.

Anderson, M. C., W. P. Kustas, C. R. Hain, C. Cammalleri, F. Gao, M. Yilmaz, I. Mladenova, J. Otkin, M. Schull, and R. Houborg (2013), Mapping surface fluxes and moisture conditions from field to global scales using ALEXI/DisALEXI, *Remote Sensing of Energy Fluxes and Soil Moisture Content*, 207-232.

Baldocchi, D. (2008), 'Breathing' of the terrestrial biosphere: lessons learned from a global network of carbon dioxide flux measurement systems, *Australian Journal of Botany*, *56*, 1-26.

Baldocchi, D., E. Falge, L. H. Gu, R. J. Olson, D. Hollinger, S. W. Running, P. M. Anthoni, C. Bernhofer, K. Davis, R. Evans, J. Fuentes, A. Goldstein, G. Katul, B. E. Law, X. H. Lee, Y. Malhi, T. Meyers, W. Munger, W. Oechel, K. T. P. U, K. Pilegaard, H. P. Schmid, R. Valentini, S. Verma, T. Vesala, K. Wilson, and S. C. Wofsy (2001), FLUXNET: A new tool to study the temporal and spatial variability of ecosystem-scale carbon dioxide, water vapor, and energy flux densities, *Bulletin of the American Meteorological Society*, *82*(11), 2415-2434.

Bi, L., P. Yang, G. W. Kattawar, Y.-X. Hu, and B. A. Baum (2011), Diffraction and external reflection by dielectric faceted particles, *J. Quant. Spectrosc. Radiant. Transfer*, *112*, 163-173.

Bisht, G., V. Venturini, S. Islam, and L. Jiang (2005), Estimation of the net radiation using MODIS (Moderate Resolution Imaging Spectroradiometer), *Remote Sensing of Environment*, *97*, 52-67.

Bouchet, R. J. (1963), Evapotranspiration re´elle evapotranspiration potentielle, signification climatique*Rep. Publ. 62*, 134-142 pp, Int. Assoc. Sci. Hydrol., Berkeley, California.

Chen, X., H. Wei, P. Yang, and B. A. Baum (2011), An efficient method for computing atmospheric radiances in clear-sky and cloudy conditions, *J. Quant. Spectrosc. Radiant. Transfer*, *112*, 109-118.

Chen, Y., J. Xia, S. Liang, J. Feng, J. B. Fisher, X. Li, X. Li, S. Liu, Z. Ma, and A. Miyata (2014), Comparison of satellite-based evapotranspiration models over terrestrial ecosystems in China, *Remote Sensing of Environment*, *140*, 279-293.

Coll, C., Z. Wan, and J. M. Galve (2009), Temperature-based and radiance-based validations of the V5 MODIS land surface temperature product, *Journal of Geophysical Research*, *114*(D20102), doi:10.1029/2009JD012038.

Ershadi, A., M. F. McCabe, J. P. Evans, N. W. Chaney, and E. F. Wood (2014), Multi-site evaluation of terrestrial evaporation models using FLUXNET data, *Agricultural and Forest Meteorology*, *187*, 46-61.

Famiglietti, C. A., J. B. Fisher, G. Halverson, and E. E. Borbas (2018), Global validation of MODIS near-surface air and dew point temperatures, *Geophysical Research Letters*, *45*, 1-9.

Fisher, J. B., K. Tu, and D. D. Baldocchi (2008), Global estimates of the land-atmosphere water flux based on monthly AVHRR and ISLSCP-II data, validated at 16 FLUXNET sites, *Remote Sensing of Environment*, *112*(3), 901-919.

Fisher, J. B., R. H. Whittaker, and Y. Malhi (2011), ET Come Home: A critical evaluation of the use of evapotranspiration in geographical ecology, *Global Ecology and Biogeography*, *20*, 1-18.

Fisher, J. B., D. D. Baldocchi, L. Misson, T. E. Dawson, and A. H. Goldstein (2007), What the towers don't see at night: Nocturnal sap flow in trees and shrubs at two AmeriFlux sites in California, *Tree Physiology*, *27*(4), 597-610.

Fisher, J. B., S. Hook, R. Allen, M. Anderson, A. French, C. Hain, G. Hulley, and E. Wood (2014), The ECOsystem Spaceborne Thermal Radiometer Experiment on Space Station (ECOSTRESS): science motivation, paper presented at American Geophysical Union Fall Meeting, San Francisco.

Fisher, J. B., F. Melton, E. Middleton, C. Hain, M. Anderson, R. Allen, M. F. McCabe, S. Hook, D. Baldocchi, P. A. Townsend, A. Kilic, K. Tu, D. D. Miralles, J. Perret, J.-P. Lagouarde, D. Waliser, A. J. Purdy, A. French, D. Schimel, J. S. Famiglietti, G. Stephens, and E. F. Wood (2017), The future of evapotranspiration: Global requirements for ecosystem functioning, carbon and climate feedbacks, agricultural management, and water resources, *Water Resources Research*, *53*, 2618-2626.

Fisher, J. B., Y. Malhi, A. C. de Araújo, D. Bonal, M. Gamo, M. L. Goulden, T. Hirano, A. Huete, H. Kondo, T. Kumagai, H. W. Loescher, S. Miller, A. D. Nobre, Y. Nouvellon, S. F. Oberbauer, S. Panuthai, C. von Randow, H. R. da Rocha, O. Roupsard, S. Saleska, K. Tanaka, N. Tanaka, and K. P. Tu (2009), The land-atmosphere water flux in the tropics, *Global Change Biology*, *15*, 2694-2714.

García, M., I. Sandholt, P. Ceccato, M. Ridler, E. Mougin, L. Kergoat, L. Morillas, F. Timouk, R. Fensholt, and F. Domingo (2013), Actual evapotranspiration in drylands derived from in-situ and satellite data: Assessing biophysical constraints, *Remote Sensing of Environment*, *131*, 103-118.

Goulden, M. L., J. W. Munger, S. M. Fan, B. C. Daube, and S. C. Wofsy (1996), Measurements of carbon sequestration by long-term eddy covariance: methods and a critical evaluation of accuracy, *Global Change Biology*, *2*, 169-182.

Halverson, G., M. Barker, S. Cooley, and S. Pestana (2016), Costa Rica agriculture: applying ECOSTRESS diurnal cycle land surface temperature and evapotranspiration to agricultural soil and water management*Rep.*

Iqbal, M. (2012), *An introduction to solar radiation*, Elsevier.

Iwabuchi, H. (2006), Efficient Monte Carlo Methods for Radiative Transfer Modeling, *Journal of the Atmospheric Sciences*, *63*(9), 2324-2339.

June, T., J. R. Evans, and G. D. Farquhar (2004), A simple new equation for the reversible temperature dependence of photosynthetic electron transport: a study on soybean leaf, *Functional Plant Biology*, *31*(3), 275-283.

Jung, M., M. Reichstein, and A. Bondeau (2009), Towards global empirical upscaling of FLUXNET eddy covariance observations: validation of a model tree ensemble approach using a biosphere model, *Biogeosciences*, *6*, 2001-2013.

Kobayashi, H., and H. Iwabuchi (2008), A coupled 1-D atmosphere and 3-D canopy radiative transfer model for canopy reflectance, light environment, and photosynthesis simulation in a heterogeneous landscape, *Remote Sensing of Environment*, *112*(1), 173-185.

Lagouarde, J., and Y. Brunet (1993), A simple model for estimating the daily upward longwave surface radiation flux from NOAA-AVHRR data, *International Journal of Remote Sensing*, *14*(5), 907-925.

Liang, X., D. P. Lettenmaier, E. Wood, and S. J. Burges (1994), A simple hydrologically based model of land surface water and energy fluxes for general circulation models, *Journal of Geophysical Research*, *99*(D7), 14415-14428.

Mallick, K., A. Jarvis, J. B. Fisher, K. P. Tu, E. Boegh, and D. Niyogi (2013), Latent heat flux and canopy conductance based on Penman-Monteith, Priestley-Taylor equation, and Bouchet's complementary hypothesis, *Journal of Hydrometeorology*, *14*, 419-442.

Mallick, K., A. J. Jarvis, E. Boegh, J. B. Fisher, D. T. Drewry, K. P. Tu, S. J. Hook, G. Hulley, J. Ardö, and J. Beringer (2014), A Surface Temperature Initiated Closure (STIC) for surface energy balance fluxes, *Remote Sensing of Environment*, *141*, 243-261.

McCabe, M. F., A. Ershadi, C. Jimenez, D. G. Miralles, D. Michel, and E. F. Wood (2016), The GEWEX LandFlux project: evaluation of model evaporation using tower-based and globally gridded forcing data, *Geosci. Model Dev.*, *9*(1), 283-305.

Michel, D., C. Jiménez, D. Miralles, M. Jung, M. Hirschi, A. Ershadi, B. Martens, M. McCabe, J. Fisher, and Q. Mu (2016), TheWACMOS-ET project–Part 1: Tower-scale evaluation of four remote-sensing-based evapotranspiration algorithms, *Hydrology and Earth System Sciences*, *20*(2), 803-822.

Miralles, D., C. Jiménez, M. Jung, D. Michel, A. Ershadi, M. McCabe, M. Hirschi, B. Martens, A. Dolman, and J. Fisher (2016), The WACMOS-ET project, part 2: evaluation of global terrestrial evaporation data sets, *Hydrology and Earth System Sciences*, *20*(2), 823-842.

Miralles, D. G., T. R. H. Holmes, R. A. M. De Jeu, J. H. Gash, A. G. C. A. Meesters, and A. J. Dolman (2011), Global land-surface evaporation estimated from satellite-based observations, *Hydrol. Earth Syst. Sci.*, *15*(2), 453-469.

Monteith, J. L. (1965), Evaporation and the environment, *Symposium of the Society of Exploratory Biology*, *19*, 205-234.

Mu, Q., M. Zhao, and S. W. Running (2011), Improvements to a MODIS global terrestrial evapotranspiration algorithm, *Remote Sensing of Environment*, *111*, 519-536.

Papale, D., and A. Valentini (2003), A new assessment of European forests carbon exchange by eddy fluxes and artificial neural network spatialization, *Global Change Biology*, *9*, 525-535.

Penman, H. L. (1948), Natural evaporation from open water, bare soil and grass, *Proceedings of the Royal Society of London Series A*, *193*, 120-146.

Potter, C. S., J. T. Randerson, C. B. Field, P. A. Matson, P. M. Vitousek, H. A. Mooney, and S. A. Klooster (1993), Terrestrial ecosystem production: a process based model based on global satellite and surface data, *Global Biogeochemical Cycles*, *7*(4), 811-841.

Prata, A. J. (1996), A new long-wave formula for estimating downward clear-sky radiation at the surface, *Quarterly Journal of the Royal Meteorological Society*, *122*(533), 1127-1151.

Price, J. C. (1977), Thermal inertia mapping: a new view of the earth, *Journal of Geophysical Research*, *82*(18), 2582-2590.

Priestley, C. H. B., and R. J. Taylor (1972), On the assessment of surface heat flux and evaporation using large scale parameters, *Monthly Weather Review*, *100*, 81-92.

Roesch, A., C. Schaaf, and F. Gao (2004), Use of Moderate-Resolution Imaging Spectroradiometer bidirectional reflectance distribution function products to enhance simulated surface albedos, *Journal of Geophysical Research*, *109*(D12), doi: 10.1029/2004JD004552.

Ryu, Y., D. D. Baldocchi, H. Kobayashi, C. van Ingen, J. Li, T. A. Black, J. Beringer, E. van Gorsel, A. Knohl, B. E. Law, and O. Roupsard (2011), Integration of MODIS land and atmosphere products with a coupled-process model to estimate gross primary productivity and evapotranspiration from 1 km to global scales, *Global Biogeochem. Cycles*, *25*(4), GB4017.

Ryu, Y., D. D. Baldocchi, T. A. Black, M. Detto, B. E. Law, R. Leuning, A. Miyata, M. Reichstein, R. Vargas, C. Ammann, J. Beringer, L. B. Flanagan, L. Gu, L. B. Hutley, J. Kim, H. McCaughey, E. J. Moors, S. Rambal, and T. Vesala (2012), On the temporal upscaling of evapotranspiration from instantaneous remote sensing measurements to 8-day mean daily-sums, *Agricultural and Forest Meteorology*, *152*(0), 212-222.

Stone, P. H., S. Chow, and W. J. Quirr (1977), July climate and a comparison of January and July climates simulated by GISS general circulation model, *Monthly Weather Review*, *105*(2), 170-194.

Su, Z. (2002), The Surface Energy Balance System (SEBS) for estimation of turbulent heat fluxes, *Hydrology and Earth System Sciences*, *6*, 85-99.

Vinukollu, R. K., E. F. Wood, C. R. Ferguson, and J. B. Fisher (2011), Global estimates of evapotranspiration for climate studies using multi-sensor remote sensing data: Evaluation of three process-based approaches, *Remote Sensing of Environment*, *115*, 801-823.

Wang, K., P. Wang, Z. Li, M. Cribb, and M. Sparrow (2007), A simple method to estimate actual evapotranspiration from a combination of net radiation, vegetation index, and temperature, *Journal of Geophysical Research*, *112*(D15107), doi:10.1029/2006JD008351.

Wind, G., S. Platnick, M. D. King, P. A. Hubanks, M. J. Pavolonis, A. K. Heidinger, P. Yang, and B. A. Baum (2010), Multilayer cloud detection with the MODIS near-infrared water vapor absorption band, *Journal of Applied Meteorology and Climatology*, *49*, 2315-2333.

Yang, F., M. A. White, A. R. Michaelis, K. Ichii, H. Hashimoto, P. Votava, A.-X. Zhu, and R. R. Nemani (2006), Prediction of continental-scale evapotranspiration by combining MODIS and AmeriFlux data through support vector machine, *Geoscience and Remote Sensing, IEEE Transactions on*, *44*(11), 3452-3461.

Zhang, L., B. Wylie, T. Loveland, E. Fosnight, L. L. Tieszen, L. Ji, and T. Gilmanov (2007), Evaluation and comparison of gross primary production estimates for the Northern Great Plains grasslands, *Remote Sensing of Environment*, *106*(2), 173-189.

Zhang, Q., X. Xiao, B. H. Braswell, E. Linder, J. Aber, and B. Moore (2005), Estimating seasonal dynamics of biophysical and biochemical parameters in a deciduous forest using MODIS data and a radiative transfer model, *Remote Sensing of Environment*, *99*, 357-371.